CHEMISTRY OF MATERIALS

ARTICLE

pubs.acs.org/cm

Citric Acid- and Ammonium-Mediated Morphological Transformations of Olivine $LiFePO_4$ Particles

Zhouguang Lu,[○,†,‡] Hailong Chen,[†] Rosa Robert,[†,§] Ben Y. X. Zhu,[†,§] Jianqiu Deng,[‡] Lijun Wu,[∥] C. Y. Chung,[*,‡] and Clare P. Grey[*,†,§]

[†]Department of Chemistry, Stony Brook University, Stony Brook, New York 11794-3400, United States

[‡]Department of Physics and Materials Science, City University of Hong Kong, Tat Chee Avenue, Kowloon, Hong Kong SAR, People's Republic of China

[§]Department of Chemistry, Cambridge University, Cambridge, CB2 1EW, United Kingdom

[∥]Center for Functional Nanomaterials, Brookhaven National Laboratory, Upton, New York 11793-5000, United States

Supporting Information

ABSTRACT: The effects of citric acid (CA) and ammonium (NH_4^+) ions on the structural and morphological transformations of olivine $LiFePO_4$ upon hydrothermal treatment are systematically investigated, as a function of reaction time, by using a combination of powder X-ray diffraction (XRD), scanning electron microscopy (SEM), transmission electron microscopy (TEM), magic-angle-spinning nuclear magnetic resonance (MAS NMR), and Fourier transform infrared absorption spectroscopy (FTIR). In the presence of both CA and NH_4^+ ions, the structures evolve from amorphous precursors to crystalline $(NH_4)FePO_4 \cdot H_2O$ and finally $LiFePO_4$. The initial olivine particles adopt an egglike shape and appear to form from the fusing of $(NH_4)FePO_4 \cdot H_2O$ plates. This metastable morphology evolves to form a mixture of cubic and rhombic particles. These particles are then etched, resulting in hollow structures and then ultimately barrel-like particles, after over 120 h of hydrothermal reaction at 180 °C. The final morphology is close to the equilibrium structure proposed by Islam et al. [Fisher, C. A. J.; Islam, M. S. *J. Mater. Chem.* **2008**, *18*, 1209]. The presence of NH_4^+ ions (as detected by FTIR) adsorbed on the surfaces of these particles, seems to slow growth along certain directions, resulting in cubic/rhombic-shaped particles. The formation of hollow particles is ascribed to the opposing effects of etching (from CA) and surface protection (from NH_4^+). The electrochemical performances vary significantly with particle shape. The hollow and roughened spindle-like particles (formed in the absence of NH_4^+ ions) exhibit superior electrochemical properties, compared to the other particles, because of their higher specific surface areas and shorter Li^+ ion diffusion lengths. The facile synthesis of olivine $LiFePO_4$ particles with very different morphologies provides an interesting platform for further fundamental investigation into the shape-dependent electrochemical performance and electrochemical lithium intercalation and deintercalation mechanisms of olivine $LiFePO_4$.

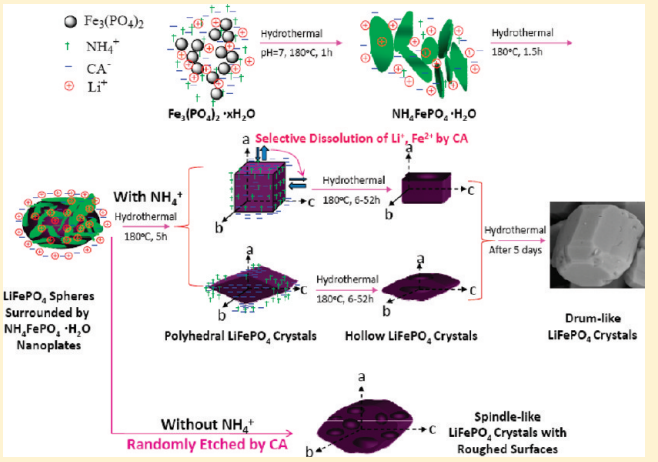

KEYWORDS: lithium ion batteries, lithium iron phosphates, shape controlled particles, hydrothermal

1. INTRODUCTION

Olivine-type $LiFePO_4$ has recently become one of the most important cathode materials for Li-ion batteries, because of its superior capacity retention, thermal stability, nontoxicity, safety, and potentially low cost. Furthermore, $LiFePO_4$ shows remarkable tolerance to overcharge and discharge, and, in this respect, is noticeably better than the commercial cathode materials currently used in Li-ion batteries.[1−4] The advantages of traditional lithium-ion batteries (i.e., high energy density, design flexibility) coupled with the excellent safety features of olivine phosphates, make $LiFePO_4$ one of the most promising electrode materials of choice for the hybrid electric vehicles (HEVs) and even electric vehicles (EVs). However, bulk, micrometer-sized $LiFePO_4$ suffers from a poor rate capability in part because of its inherent low electronic conductivity ($\sim 10^{-9} - 10^{-10}$ S cm^{-1}) and possibly due to its one-dimensional (1D) Li^+ ionic conductivity.[5,6]

Received: January 21, 2011
Revised: April 1, 2011
Published: May 12, 2011

 © 2011 American Chemical Society

In the past decade, much effort has been devoted to improve the rate performance of $LiFePO_4$. Notable approaches include (i) surface coating of the $LiFePO_4$ particles with a thin layer of conductive carbon,[7−9] (ii) making homogeneous composites with conductive polymers,[10,11] (iii) adding surface layers/nanoparticles of highly conductive inorganic materials (such as Ag,[12] Fe_2P,[13] and RuO_2[14]), to improve the electronic connection between the carbon conductive matrix and $LiFePO_4$, (iv) the creation of a fast Li^+-ion conducting coating on the surface of ultrafine $LiFePO_4$ nanoparticles,[15] and (v) aliovalent doping.[16] Another approach is to fabricate ultrafine $LiFePO_4$ nanoparticles via wet-chemical routes to shorten the diffusion distance for both Li^+ ions and electrons and thereby substantially improve the rate capability.[17,18] Shortening of diffusion pathways has also been achieved by forming microporous or mesoporous structures inside large primary $LiFePO_4$ particles.[19−21]

Despite considerable progress in this field, numerous questions related to the fundamental origin by which $LiFePO_4$ functions remain to be answered. Various models have been proposed to explain the lithiation and delithiation mechanism, such as the core/shell model,[2,22] the modified shrink-core model,[23] the alternating phase boundaries model,[24] the spinodal-decomposition model,[25] the mosaic model,[26] and the domino-cascade model.[27] The electrochemical properties of $LiFePO_4$ can be highly dependent on shape and size,[28−32] and at least some of the differences between the models can partially be ascribed to the fact that these models are derived from experiments on different samples, which have quite different particle size, morphology, defects, and surface chemistry. For example, although theoretical simulations[5,6,28,33] and neutron diffraction experiments[34] on polycrystalline powders have revealed that lithium mobility predominantly occurs in the 1D channels along the *b*-direction, ionic conductivity experiments on large single crystals showed that the conductivity is larger in the *ac*-plane than in the perpendicular planes.[35] However, a later lithium-ion conductivity study of a $LiFePO_4$ single crystal showed that the lithium-ion diffusion is largely confined to the 1D tunnels along the *b*-axis.[36] This discrepancy presumably results from the fact that the large single crystals may have more defects per tunnel (since the tunnels are longer). Even a single defect in a 1D channel can lower the conductivity significantly as it blocks the tunnels.[37] Recently, Wagemaker et al.[30] have predicted that the solubility limits and the equilibrium compositions are not only dependent on the particle size, but they are also surprisingly sensitive to the particle shape. Moreover, considering the highly anisotropic nature of the $LiFePO_4$ crystal structure, control of the particle shape may be as important as size control.[33,38,39]

Given the importance of particle shape on the performance of $LiFePO_4$, a range of synthesis techniques have been used to prepare olivine $LiFePO_4$ with a variety of particle morphologies and size distributions. For instance, $LiFePO_4$ nanowires have been synthesized via a surfactant (nitrilotriacetic acid (NTA))-assisted hydrothermal method.[40] Similarly, rodlike $LiFePO_4$ nanocrystallites have been synthesized by ionothermal[41] and microwave-assisted hydrothermal techniques.[42] $LiFePO_4$ crystallites have also been observed as platelets,[24,43] rectangular prisms,[41] and spindle-like,[31,44,45] diamond-like,[44,46,47] block-like,[29,31,41,44,48] spherical-like,[49−51] core/shell-like,[52] hollow-like,[21,53] and bundle-like[31,44,48,54] particles. Hydrothermal reactions represent a versatile approach to manipulate nanoparticle morphologies of $LiFePO_4$ at low temperatures.[24,29,31,42,45] The particle geometries of the products are highly dependent on the experimental parameters, the addition of organic molecules, such as glucose,[42] citric acid (CA),[24,29] ethylene glycol (EG),[43] sugar, ascorbic acid,[29,55] and hexadecyltrimethylammonium bromide (CTAB),[56] etc., in particular acting as shape controllers. The introduced organics can also serve as precursors for either in situ carbon coating during hydrothermal treatment, or post-hydrothermal carbon coating by annealing and can prevent the oxidation of Fe^{2+} to Fe^{3+}. CA strongly complexes metal ions, and it has been widely used as a chelating agent in sol−gel routes (the so-called Pechini method) to prepare $LiFePO_4$ nanoparticles.[57] In this work, we show that the presence of CA and NH_4^+ in the hydrothermal reaction system has a profound effect on the particle morphology of $LiFePO_4$ and a series of olivine $LiFePO_4$ particles with well-defined and novel geometries, can be obtained by carefully adjusting the hydrothermal reaction parameters. We first present an X-ray diffraction (XRD) study of the hydrothermal reaction to identify which phases are present at different times. The products are then investigated by transmission electron microscopy (TEM) and scanning electron microscopy (SEM), to track the change in particle morphology, as a function of the hydrothermal reaction period. The formation mechanism of these novel-shaped $LiFePO_4$ particles is studied in some detail using XRD, SEM, TEM, Fourier transform infrared spectroscopy (FTIR), as well as by nuclear magnetic resonance (NMR). The electrochemical properties of these $LiFePO_4$ particles are then investigated and correlated with their particle morphologies and sizes.

2. EXPERIMENTAL SECTION

2.1. Sample Preparation. Unless specially indicated, the procedure used to prepare $LiFePO_4$ is as follows. In the first step, 0.005 mol of $(NH_4)_2Fe(SO_4)_2\cdot 6H_2O$, 0.005 mol of $(NH_4)H_2PO_4$, and 0.015 mol of $LiOH\cdot H_2O$ were thoroughly dissolved in 3 × 10 mL deionized water at room temperature to prepare clear Fe^{2+}, PO_4^{3-}, and Li^+ solutions, respectively. The $(NH_4)_2Fe(SO_4)_2\cdot 6H_2O$ and $(NH_4)H_2PO_4$ solutions then were mixed under vigorous stirring and a cloudy green solution was formed. White precipitates were instantly produced after the subsequent addition of the LiOH solution. The color of the precipitates gradually transformed from white to greenish-yellow with further addition of LiOH. The final concentration ratio of $[Fe^{2+}]$:$[PO_4^{3-}]$:$[Li^+]$ was adjusted to be 1:1:3 and the corresponding pH value was ∼8.5. Then, 0.0025 mol of CA was rapidly added to this mixture under vigorous stirring. At this step, the color of the solution changed from greenish-yellow to green and the pH value dropped to ∼7. After stirring under nitrogen for ∼10 min, the slurry was quickly transferred into a Teflon vessel (volume 50 mL) in a stainless steel autoclave. The autoclave was then purged with nitrogen, sealed, and placed in an oven held at a constant temperature of 180 °C and kept under hydrothermal conditions for 15 h. Subsequently, the autoclave was slowly cooled to room temperature and the resulting off-white precipitates were filtered and thoroughly washed with deionized water and acetone several times, and dried at 80 °C for 12 h under vacuum. To investigate the formation process of the $LiFePO_4$ particles, we conducted parallel experiments by keeping all the parameters constant and only changing the hydrothermal reaction time. For the sake of comparison, phase-pure $NH_4FePO_4\cdot H_2O$ was prepared. The synthesis procedure and the corresponding XRD result for this phase are shown in Figure S1 in the Supporting Information.

2.2. X-ray Diffraction. All the samples were characterized by X-ray diffraction (XRD) in a $\theta/2\theta$ configuration using a Rigaku Mini-Flex powder diffractometer equipped with a Cr-target X-ray tube (Cr Kα radiation, λ = 2.29 Å). For easy comparison, all the patterns were converted to those corresponding to a Cu $K\alpha_1$ wavelength (λ = 1.5406 Å). The cell parameters were extracted from refinement using the Jade 5 software.

2.3. Fourier Transform Infrared (FTIR) Spectroscopy. FTIR absorption spectra were recorded with a Fourier transform interferometer (Perkin−Elmer, model Spectrum 100) from 400 cm^{-1} to 4000 cm^{-1} at a spectral resolution of 2 cm^{-1}. The samples were ground to fine powders and homogeneously mixed with dry KBr powder in a 1:200 (wt) proportion and then thin pellets were prepared by cold pressing.

2.4. MAS NMR Spectroscopy. ^{7}Li and ^{31}P magic-angle-spinning (MAS) NMR spectroscopy was performed on the samples with a double-resonance 1.8 mm probe on a CMX-200 spectrometer with a magnetic field strength of 4.7 T. A spinning speed of 38 kHz and a rotor-synchronized spin−echo sequence ($\pi/2-\tau-\pi-\tau$-aq) were used to acquire the spectra. The ^{7}Li spectra were collected at an operating frequency of 77.71 MHz with $\pi/2$ pulses of 2.75 μs and an acquisition delay time of 0.2 s. The spectrum was referenced to 1 M ^{7}LiCl in H_2O at 0 ppm. For the ^{31}P MAS NMR spectroscopy, the observed signals were very broad and, thus, the entire spectrum could not be excited simultaneously. To overcome this problem, separate spectra were acquired as a function of irradiation frequency, starting at a carrier frequency of 80.94 MHz, which corresponds to the Larmor frequency of the standard ^{31}P external reference (H_3PO_4 aqueous solution, set at 0 ppm). The carrier frequency was moved in uniform steps of 650 kHz, and the resulting spectra were normalized to the same scan number and mathematically added up to give a quantitative spectrum corresponding to each sample. For all frequencies, the $\pi/2$ pulse width was fixed at 2.2 μs and the delay time was set at 0.1 s.

2.5. Electron Microscopy. The morphology of the products was characterized using a Hitachi H-800 TEM microscope operating at 200 kV, a JEOL-4000 high-resolution TEM microscope (200 kV), a LEO-1550 SEM microscope, and a JEOL JSM-6334F SEM microscope.

2.6. Electrochemical Characterization. Electrochemical characterization was performed using Swagelok-type cells. Positive electrodes were prepared by shock-milling a powder mixture containing 80 wt % active material with 20 wt % carbon black. Some samples were carbon-coated by mixing the LFP particles with 20 wt % sucrose (corresponding to ~5 wt % conductive carbon) and annealing at 600 °C for 2 h under argon (>99.99) gas.

The cells were assembled in an argon-filled glovebox with lithium metal foil as the anode, 10 mg of the carbon/active material mixture, one sheet of glass fiber disk, and one layer of Celgard 2025 (Celgard, Inc., USA) as the separators, and $LiPF_6$ (1M) dissolved in ethylene carbonate (EC)/dimethyl carbonate (DMC) mixture (1/1 w/w) as the electrolyte. Galvanostatic electrochemical experiments were carried out with a model BT 200 battery cycler (Arbin Instruments, College Station, TX) at room temperature.

3. RESULTS AND DISCUSSION

3.1. Crystal Phase Transformations. *3.1.1. XRD.* XRD patterns were taken of powders extracted from the $(NH_4)_2Fe(SO_4)_2\cdot 6H_2O$, $(NH_4)H_2PO_4$, $LiOH\cdot H_2O$, and CA reaction mixture, as a function of time. The pattern of the greenish-yellow precipitate (0-h sample), obtained after mixing all the reagents and stirring for 10 min, just before transferring it to the hydrothermal autoclave, reveals an amorphous product [see Figure 1 and Figure S2a in the Supporting Information]. The presence of a broad peak at a low 2θ angle (centered at $2\theta \approx 6.9°$) may be an indication of a mesosized structure or a lamella-like structure in the precipitated precursor. After the precursor was calcined at 600 °C for 2 h under a 95% Ar/5% H_2 gas atmosphere, sharper Bragg reflections were observed, which are assigned to an $Fe_3(PO_4)_2$ phase [see Figure S2b in the Supporting Information], indicating that the precursor phase mainly contains iron and phosphorus. The product was black, presumably due to carbon produced from the decomposition of CA, suggesting that some amorphous CA−iron compounds are also present in the precipitate. Our experiments are consistent with the literature,[29,58] where a highly disordered hydrated iron(II) phosphate was formed after mixing Fe^{2+} with PO_4^{3-} in the presence of NH_4^+.

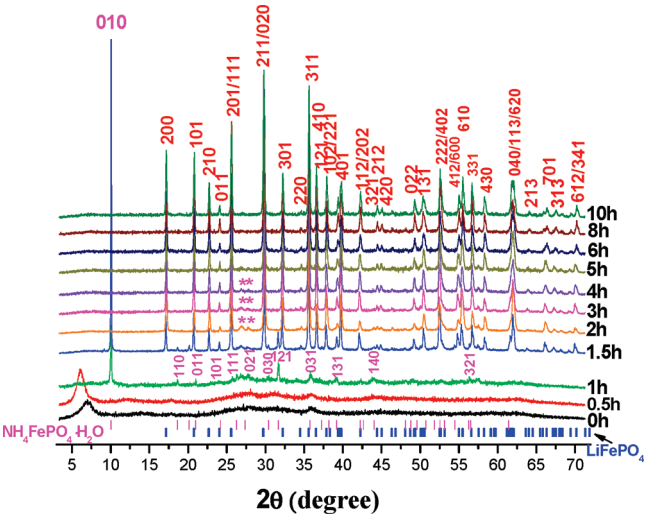

Figure 1. Evolution of the XRD patterns of the products extracted from the reaction mixture, as a function of hydrothermal reaction time. The bottom blue and pink bars correspond to the Bragg reflections for $LiFePO_4$ (JCPDS File Card No. 832092) and $NH_4FePO_4\cdot H_2O$ (JCPDS File Card No. 450424), respectively. The asterisks signify the reflections from $Fe_3(PO_4)_2\cdot 8H_2O$ (JCPDS File Card No. 300662).

Hydrothermal treatment at 180 °C for 0.5 h did not result in a noticeable change in the XRD pattern of the green precursor (the red pattern in Figure 1), except that the reflection observed at 6.9° 2θ has shifted to a lower 2θ value ($2\theta = 6.0°$). After 1 h, this low-angle reflection has disappeared and Bragg reflections from crystalline phases start to become visible (the green pattern in Figure 1), in addition to the significant amorphous contribution. The crystalline component can be indexed to $NH_4FePO_4.H_2O$ (NFP) in the $Pmn2_1$ space group.[59] After 1.5 h at the same temperature, the product now consists of a mixture of $LiFePO_4$ (LFP) and NFP (the blue pattern in Figure 1). The very strong peak at 10.0° 2θ corresponds to the (010) reflection of NFP. Its high intensity is presumably due to the preferred orientation that arises from the thin platelet morphology of the as-grown NFP particles,[60] but may also be due to disorder between the phosphate layers of this structure which broadens the other reflections. The formation of NFP as an intermediate prior to the formation of the olivine LFP phase was also seen earlier by Ellis et al.[29] The crystal structure of LFP [see Figures S3a, S3c, and S3e in the Supporting Information, space group *Pnma*] is comprised of corner-shared FeO_6 octahedra and PO_4 tetrahedra, and edge-shared LiO_6 octahedra,[1] while in NFP, the Fe^{2+} ions are coordinated in a severely distorted octahedron by five PO_4 tetrahedra and one H_2O molecule, the sheets being separated by NH_4^+ ions.[59] Thus, the connectivity of the Fe−O and P−O polyhedra in the (100) plane of LFP and the (010) plane of NFP [see Figures S3b, S3d, and S3f in the Supporting Information, space group $Pmn2_1$] are identical and ion exchange of NH_4^+ with Li^+ can result in the interconversion between the two phases as the hydrothermal treatment proceeds.

The XRD pattern of the 2-h sample is dominated by reflections from LFP. Weak signals from the vivianite $Fe_3(PO_4)_2\cdot 8H_2O$ phase can be seen (magenta asterisks, Figure 1), but their intensity decreases with reaction time. After 6 h, phase-pure

dx.doi.org/10.1021/cm200205n |*Chem. Mater.* 2011, 23, 2848–2859

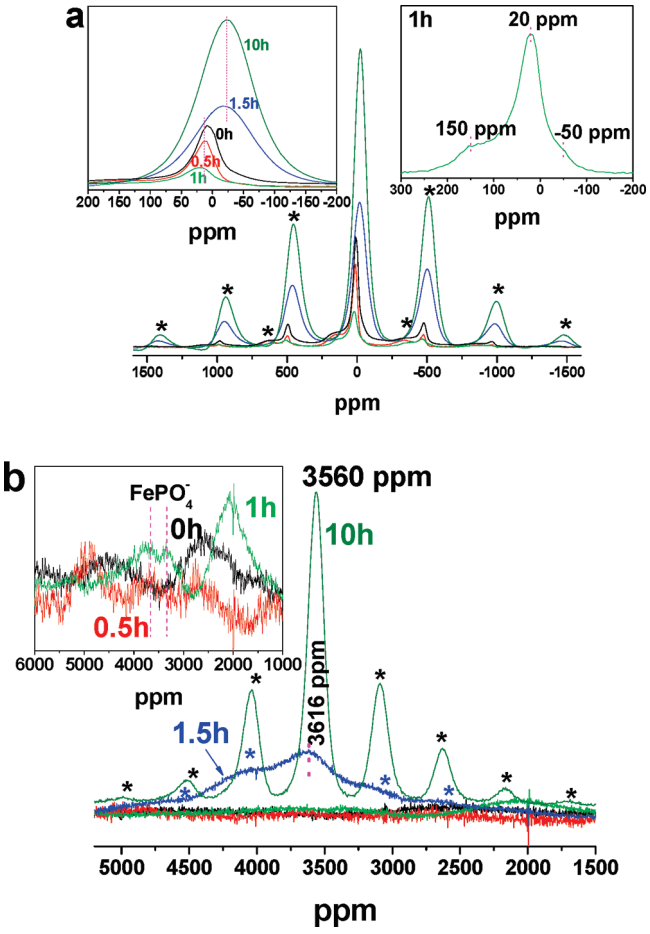

Figure 2. (a) ^{7}Li and (b) ^{31}P MAS NMR spectra of the solid phases extracted from the reaction mixture, as a function of hydrothermal reaction time. The insets in panels a and b show the expansions of the isotropic resonances (^{7}Li) and the spectra of the 0 to 1 h samples (^{31}P), respectively. The isotropic resonances and spinning sidebands are marked with shifts and asterisks, respectively. All the spectra have been normalized to acquisition number and material mass.

LFP is observed, the increase of reaction time serving only to affect the particle size and morphology, as described below.

Analysis of the cell parameters shows that the olivine phase in the 1.5-h sample has a larger cell volume (292.71 Å^3) than those reported in the literature for $LiFePO_4$ prepared via hydrothermal synthesis (291.22 Å^3,[29] 291.3 Å^3[54]). Since the cell volume is generally considered as a measure of the cation disorder,[54] this may indicate some disorder of the Li/Fe atoms in the as-formed $LiFePO_4$ phase in the 1.5-h sample. The cell volume decreases as the synthesis time increases from 1.5 h (292.71 Å^3) to 5 h (291.76 Å^3), the last value being in good agreement with values found for well-crystallized $LiFePO_4$ materials.[54] A longer hydrothermal synthesis time led to cell volume values close to 291 Å^3 (i.e., 290.95 Å^3 at 10 h and 290.86 Å^3 at 120 h), which are in the range of those observed for $LiFePO_4$ samples prepared via hydrothermal synthesis.[29,54]

3.1.2. NMR. NMR spectroscopy was used to follow the phase formations and transformations, as a complement to the long-range structural XRD data. The ^{7}Li spectra of the samples treated for 0−1 h (Figure 2a) contain two resonances at ∼150 and ∼20 ppm, which decrease in intensity with reaction time, indicating that they are associated with some intermediates in the reaction process. The ^{7}Li signals confirm the presence of lithium in the precursor phases, although, based on the relative intensity of the signals of the samples treated for <1.5 h and that of the single-phase sample (10 h), the lithium content is low. The decrease in Li intensity from 0 to 1.5 h correlates with the decrease in the highly disordered phase, as probed by XRD, and not with the formation of NFP, indicating that these NMR signals are not due to partial ion exchange (of Li^+ for NH_4^+) of this phase. The nonzero value of the observed shifts indicates that the Li^+ is directly bound to one or more oxygen atoms that are coordinated to iron, and is not due to Li^+ in an outer-sphere complex on the surface of the iron phosphate particles. In our earlier studies, we have found that Li−O−Fe^{III} interactions lead to larger positive shifts, as observed in oxides such as $LiFeO_2$ (∼300−550 ppm), phosphate phases such as $Li_3Fe_2(PO_4)_3$ (∼60−190 ppm), and for Li^+ bound to the surfaces of various FeOOH polymorphs (30−150 ppm).[61−63] In contrast, smaller shifts, which are often negative in sign, are seen for Fe(II)-containing materials. As an example, a shift of −8 ppm to −65 ppm is normally seen for $LiFePO_4$.[62,64−68] At this point in the reaction, there is little evidence for substantial Fe^{3+} concentrations (although we cannot rule out the possibility that the weak 150 ppm resonance may be associated with Fe^{3+}) and we assign the 20 ppm environments to Li coordinated to the highly disordered iron(II) phosphate framework. For the 1-h sample, in addition to the two resonances with positive shifts, a small resonance at −50 ppm appears (right inset of Figure 2a), which is assigned to Li in olivine-like local environments. At this stage, no LFP is seen by XRD, suggesting that either the phase is present in low concentrations, the phase is disordered, or (and) this signal may correspond to some lithiation of the NFP phase. After 1.5 h, a resonance centered at approximately −20 ppm can be observed, which corresponds to a typical resonance from LFP.[67]

No significant ^{31}P signals are seen in the ^{31}P spectra until 1.5 h (Figure 2b). However, a very weak, broad signal centered at ∼2500 ppm can be observed for the 0-h and 0.5h samples in an enlargement of the spectra (left inset of Figure 2b), which moves to ∼2000 ppm after 1 h. These broad peaks are tentatively assigned to a highly disordered Fe-, P-, and Li-containing phase, the disorder in the sample leading to a broad distribution of local environments and magnetic interactions, resulting in resonances spreading over a very large spectral range. Since NMR is sensitive to short-range structure (ordering), even in the amorphous state, the NMR results indicate that the product at 0 h is not even locally ordered and does not, for example, consist of nanoparticles of specific phase such as $Fe_3(PO_4)_2 \cdot 8H_2O$ or NFP.

The ^{31}P resonances grow and sharpen as the hydrothermal reaction continues, suggesting enhanced ordering. A signal at ∼3600 ppm, as highlighted by the magenta dashed lines, is observed after 0.5 h. Resonances in this frequency range grow in intensity and a resonance at 3616 ppm is clearly seen in the 1.5-h product. After 2 h (not shown), a sharp resonance is observed at 3560 ppm, which is similar to that of the 10-h product, and is characteristic of olivine-like local environments.[67] The observation of resonances in this frequency range from 0.5 h onward is consistent with the ^{7}Li NMR, where a resonance in the olivine shift range is seen from 0.5 h. However, given that the diffraction pattern of the 1-h sample is dominated by the NFP (semi)crystalline phase, it is possible that the 3600 ppm resonance in the spectrum of the 1-h sample, and a component of the broader resonance of the 1.5-h sample, is due to disordered NFP and/or partially Li-exchanged NFP. This is consistent with the similar local environments for P, in terms of the connectivity with Fe, of the LFP and NFP materials. However, the

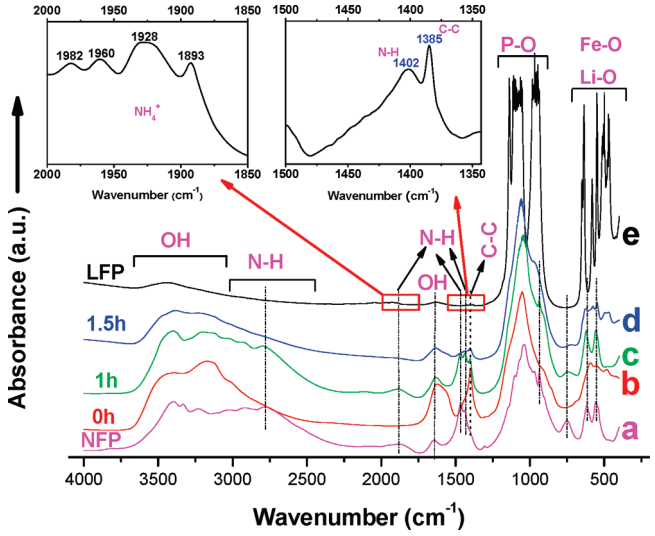

Figure 3. FTIR absorption spectra of (a) $NH_4FePO_4 \cdot H_2O$ (NFP), and the samples extracted from the hydrothermal reaction mixture after (b) 0, (c) 1, (d) 1.5, and (e) 15 h (labeled as LFP). The top-left insets show the zooms of the spectra between 2000 and 1850 cm^{-1} and 1500–1343 cm^{-1} for the 15-h LFP sample.

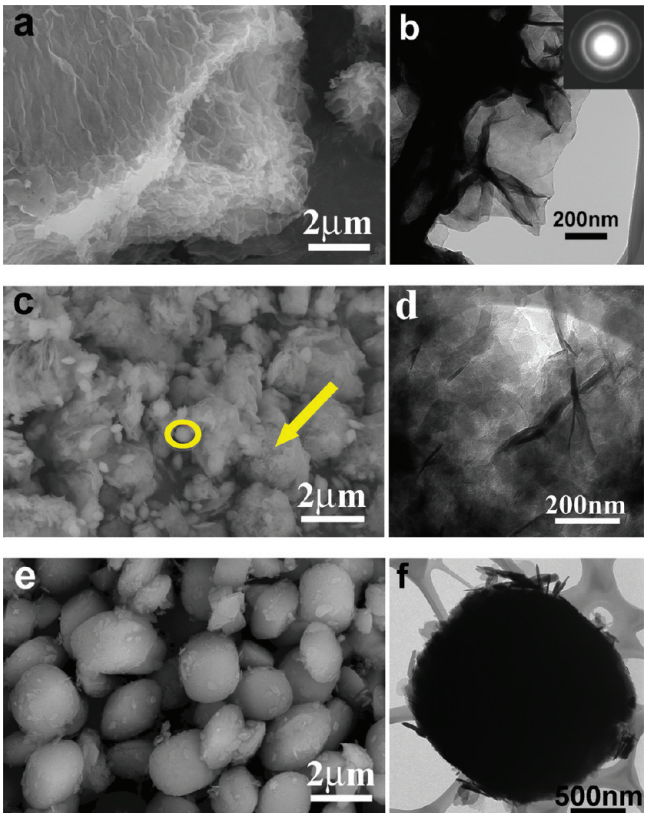

Figure 4. SEM images of the solid phases extracted from the reaction mixture after hydrothermal treatment for (a) 0 h, (c) 1 h, and (e) 1.5 h. Panels b, d, and f shows the corresponding TEM images of the samples depicted in panels a, c, and e, respectively. The inset in panel b shows the corresponding SAED pattern, demonstrating the amorphous nature of the precursor prior to the hydrothermal reaction.

crystalline NFP prepared in the absence of Li^+ for the FTIR studies gives rise to a resonance at approximately 5000 ppm, confirming that the NFP in the 1–1.5 h sample is not crystalline.

3.1.3. FTIR. The structural changes have also been investigated by FTIR absorption experiments (see Figure 3). Strong water bending modes at 1634 cm^{-1} and O–H stretches at 3600–3000 cm^{-1} [69,70] are obvious in the early stages (up to 1.5 h), suggesting that crystalline water is present. These signals are relatively weak in the $LiFePO_4$ (15 h) spectrum; the signals now presumably arise because of H_2O molecules bound to the surfaces of the $LiFePO_4$ particles. The absorptions observed at 3000–2500, 1886, and 1460 cm^{-1} can be attributed to the NH_4^+ N–H stretching mode[69,71] and the bands at ~1390 cm^{-1} are associated with ν(C–C) vibrations.[72] The strong absorption peaks extending from 800 cm^{-1} to 1250 cm^{-1} are assigned to PO_4^{3-} stretching modes,[73,74] while the strong absorption bands located between 500–700 cm^{-1} can be assigned to the vibrations of Fe–O and Li–O units, based on earlier studies.[73,74]

A comparison of the 0-h sample (Figure 3b) and the NFP sample (Figure 3a) indicates that NH_4^+ is not present to any great extent in the 0-h sample, further confirming that the as-precipitated amorphous precursor is mainly comprised of a highly amorphous iron(II) (hydrated) phosphate phase. The strong C–C signals indicate that the precipitate also contains a substantial amount of CA/citrate ions. The spectrum of the 1-h sample is very similar to that of NFP, consistent with the XRD results (see Figure 1). Organic phases are also present. The FTIR spectrum of the 1.5-h sample contains many of the characteristic PO_4^{3-} and Fe–O features of olivine $LiFePO_4$;[72–74] however, the bands are much broader, which is consistent with the disorder, as seen by NMR, and the presence of the structurally related NFP. A well-resolved olivine FTIR spectrum is seen in the 15-h sample (Figure 3e).[72–74] Interestingly, very weak signals from O–H, N–H as well as C–C can still be seen, as shown in the inset of Figure 3, indicating the presence of some CA and NH_4^+ species presumably remaining on the surfaces of the as-formed $LiFePO_4$ crystallites.

3.2. Morphological Transformations. *3.2.1. Particle Morphology Prior to the Formation of $LiFePO_4$.* Figures 4a and 4b show typical SEM and TEM images of the greenish-yellow precursors collected before hydrothermal treatment. The precursor has an amorphous lamellar structure, as indicated by the SAED pattern (see inset of Figure 4b), which is consistent with the XRD result (see Figure 1) and the NMR result (Figure 2). Hydrothermal reaction for 0.5 h has little effect on the morphology of this precursor (results are not shown). However, after 1 h, more-compact spherical nanocrystallites with mean diameters of 400 nm (indicated by a circle in Figure 4c), as well as very loose and fluffy aggregates with an average diameter of ~2 μm (indicated by an arrow in Figure 4c), were observed (Figure 4c). The TEM image in Figure 4d suggests that the loosely aggregated particles consist of ultrathin platelet-like nanoparticles and nanosheets. After 1.5 h at the same temperature, fairly uniform egg or pebble-like particles with mean diameter of 1–1.5 μm were produced [Figure 4 (e) and Figures S4a and S4c in the Supporting Information]. High-magnification SEM and TEM images, as shown in Figure 4f and Figure S4d in the Supporting Information, reveal that the egglike particles are dense particles with very thin nanoplates covering their surfaces. The sizes of the nanoplates range from a few nanometers to 100 nm. The SAED pattern of the nanoplates (Figure S4e in the Supporting Information) can be indexed to NFP, the most exposed face of the nanoplates corresponding to the (010) plane.

3.2.2. Formation of Cubic and Rhombic Shaped Particles. When the reaction time was extended to 2 h, the egg-shaped

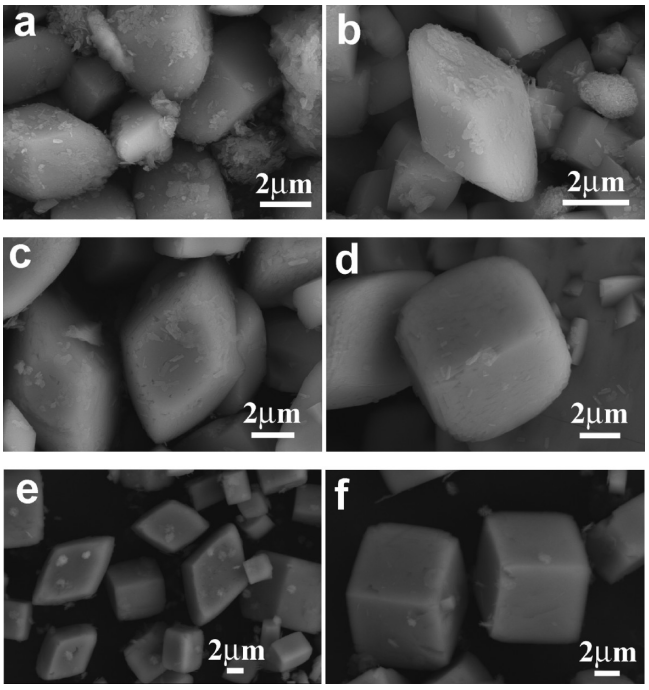

Figure 5. SEM images of the $LiFePO_4$ products obtained after hydrothermal reaction for (a, b) 2 h, (c, d) 3 h, and (e, f) 5 h.

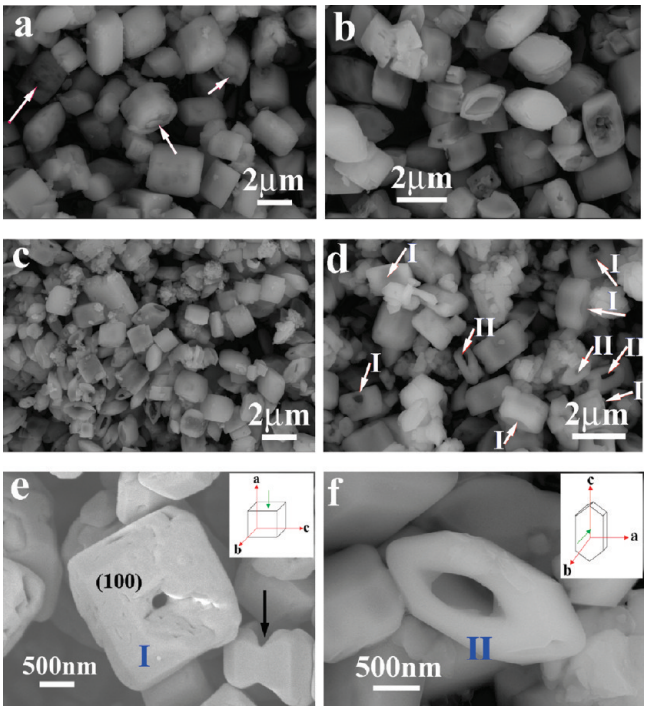

Figure 6. SEM images of the product after hydrothermal reaction for (a) 6, (b) 8, (c) 10, and (d) 15 h. The arrowed features labeled I and II in panel d indicate the cubic and truncated rhombic-shaped hollow particles, respectively. (e, f) SEM images of single cubic and truncated rhombic-shaped hollow particles, respectively. Insets in panels e and f show the schematic morphologies of the cubic and truncated rhombic-shaped hollow particles, respectively. The green arrows in these insets indicate the direction of the holes, as determined from the TEM results shown in Figure 7.

particles grow and evolve into rhombic-shaped particles with mean edge lengths of 1.5 μm, thicknesses of ~1 μm, and lengths of ~2 μm, as revealed from Figures 5a and 5b, and Figure S5a in the Supporting Information. The rhombic particles exhibit rough surfaces, presumably because of the presence of some residual NFP flakes. $Fe_3(PO_4)_2 \cdot 8H_2O$ is also detected by XRD (Figure 1, 2-h samples), which is presumably present as some of the less regularly shaped precipitates (see Figure 5a). Some more egg-shaped particles remain in the product at this point. Many of the rhombic particles have grown into cubic-shaped particles after 3 h (see Figures 5c and 5d, and Figure S5b in the Supporting Information). The mean edge length of the cubes is ~5 μm, which is larger than those of the rhombic particles (2-h sample). The particles that retain their rhombic morphology increase in size (now ~4 μm × ~2 μm × ~5 μm). Both the cubic and rhombic particles are rounded on the edges as well as the corners. The cubic and rhombic particles coexist in the 4-h product (see Figure S5c in the Supporting Information) as well as the 5-h products (see Figures 5e and 5f, and Figure S5d in the Supporting Information). However, the cubic-shaped particles become more prominent as the reaction proceeds (see Figure S5 in the Supporting Information). Furthermore, as the hydrothermal reaction proceeds, the particles display much more regular shapes with smoother surfaces and sharper edges and corners, while there is no significant change in the mean particle size.

3.2.3. Formation of Hollow Structured Particles. The SEM images of the product after hydrothermal reaction for 6 h, as shown in Figure 6a and Figure S6a in the Supporting Information, reveal that the particles undergo significant morphology changes, compared to the 5-h product (see Figures 5e and 5f). First, the particle size is now smaller (~2 μm) and second, the particles appear less regular in shape. Third, as indicated by arrows in Figure 6a, a concave structure is observed on the faces of some particles. Moreover, the corners and edges of the particles are highly truncated. After extending the hydrothermal reaction to 8 h, the hollowing out of the particles becomes more pronounced without significant change in the particle size, as revealed in Figure 6b and Figure S6b in the Supporting Information.

The number of concave particles substantially increases upon further increasing the reaction time to 10 h. Some of the particles seem to have a hollow structure and the mean particle size has slightly decreased, as revealed in Figure 6c and Figure S6c in the Supporting Information. After 15 h, most of the particles have transformed to hollow structures, as shown in Figure 6d and Figure S6d in the Supporting Information, along with some irregular ultrafine nanoparticles. High-magnification SEM images of single particles in Figure 6e and 6f give further insight into the morphology of the hollow particles. There are mainly two types of hollow particles, as highlighted in Figure 6d. One exhibits a cubic shape (I) (with highly truncated edges and corner) with a hole in the center of one face that runs through the entire particle (see Figure 6e). The edge length of the cubes is in the range of 1.5−2 μm. Indexing of the TEM SAED patterns (Figures 7a and 7b) of typical cubic-shaped hollow particles suggests that each particle is a LFP single crystal with (100), (010) and (001) faces and holes along the [100] direction. The second type of hollow particle (II) has a fat, truncated rhombic-like morphology with the holes being perpendicular to the hexagonal face (see Figure 6f). The TEM and SAED patterns in Figures 7c and 7d of the truncated rhombic-shaped hollow particles show that the rhombic facets are (010) planes and that the hole is along the [010] direction. These particles are also single crystalline in nature.

dx.doi.org/10.1021/cm200205n |*Chem. Mater.* 2011, 23, 2848–2859

3.2.4. Growth Mechanisms of the $LiFePO_4$ Particles with Different Morphologies. Based on the above observations, a mechanism for the formation of the $LiFePO_4$ particles with various geometries is proposed, as schematically illustrated in Figure 8. Here, we focus on analyzing the formation process of the hollow particles:

(I) In the precursors before the hydrothermal reaction, amorphous iron phosphate nanoparticles precipitate because of their low solubility in the solution, which, along with CA and Li^+ ions, assemble into lamella mesoporous structures.

(II) At the beginning of the hydrothermal reaction, the amorphous iron phosphate phase reacts with NH_4^+ in the stock solution to form highly oriented NFP nanoplates, with the large facets corresponding to the (010) planes, in agreement with the literature.[69,75]

(III) Ion exchange of NH_4^+ with Li^+ ion occurs between 1 h and 3 h to form LFP nanoplates. The ultrafine LFP nanoplates stack together to form large spherical aggregates, driven by surface energy minimization of the dispersed particles.[41,51] Dissolution−recrystallization processes continue throughout the hydrothermal reaction presumably assisted by the CA, with the dense egglike LFP particles forming first from the nanoplates.

(IV) The NH_4^+ concentration now increases, as the ions that were originally trapped in the NFP have now been released. The egglike structures do not represent a stable morphology under these conditions, and the particles transform to either rhombic or close-to-cubic morphologies. The grain sizes grow via Ostwald ripening.[41]

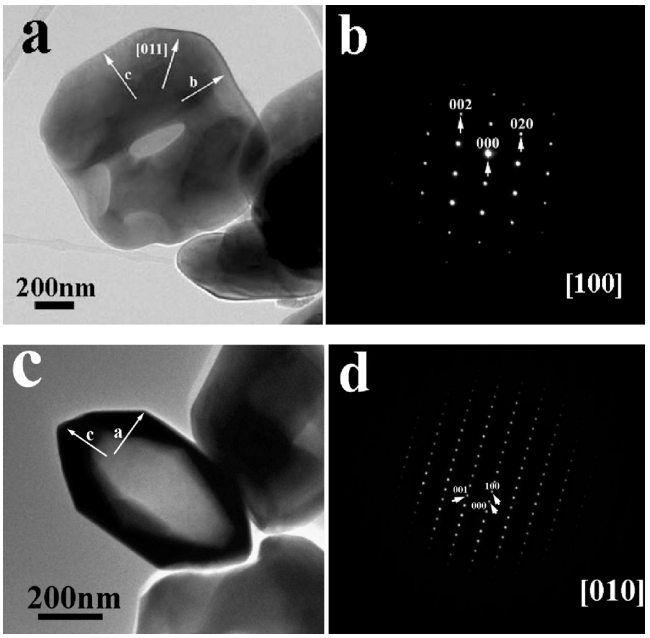

Figure 7. (a, c) Typical TEM images of single cubic particles (panel a) and truncated rhombic-shaped hollow particles (panel c). (b, d) Corresponding SAED patterns of the cubic and truncated rhombic-shaped hollow particles, along the [100] direction (panel b) and the [010] direction (panel d).

Several groups have reported the hydrothermal synthesis of single-crystalline LFP particles with highly anisotropic morphologies (for instance, thin hexagonal platelets,[24,29] rectangular prisms,[41] diamond-like[31,44−48,76] and rods[31,41−43]). Most of these single-crystalline particles are elongated along the (001) direction, indicating favorable crystal growth along the *c*-direction of the olivine $LiFePO_4$ under normal hydrothermal reactions.[77] Based on semiempirical calculations of surface energies, Islam et al.[28] have

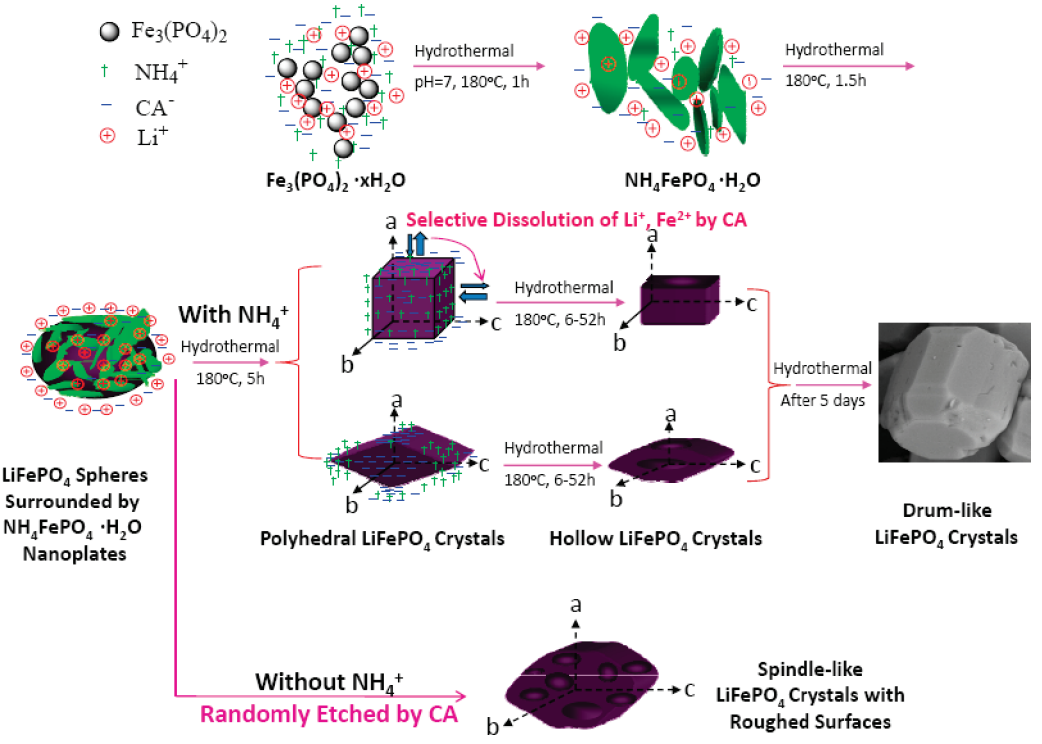

Figure 8. Schematic illustration showing the effects of time and the presence of citric acid (CA) and ammonium ions (NH_4^+) on the morphological transformations of $LiFePO_4$ particles during the hydrothermal reaction.

dx.doi.org/10.1021/cm200205n |*Chem. Mater.* 2011, 23, 2848–2859

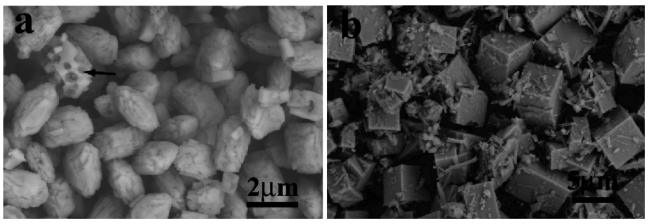

Figure 9. Typical SEM images of the $LiFePO_4$ products synthesized in the absence of (a) NH_4^+ and (b) CA. In panel a, the experimental parameters were $[FeSO_4]$ = 0.1 M, $[KH_2PO_4]$ = 0.1 M, [LiOH] = 0.3 M, [CA] = 0.05 M, pH ~7, 180 °C, 15 h. In panel b, the experimental conditions for $[NH_4^+]$ = 0.3 M, $[Fe^{2+}]$ = 0.1 M, $[Li^+]$ = 0.2 M, pH ~7, 180 °C, 15 h.

suggested that the favorable growth morphology under mild hydrothermal conditions would be an anisotropic elongated (close to) hexagonal prism terminated by (010), (100), and (101) faces. Ceder et al.[33] have calculated the thermodynamic equilibrium shape of $LiFePO_4$ crystals via a Wulff construction, utilizing density functional theory (DFT) calculations, with the two low-energy surfaces (010) and (201) dominating the Wulff shape and comprising almost 85% of the surface area. Neither of these two theoretically predicted morphologies are seen in the early stages of the reaction, in the presence of CA and NH_4^+. Instead, the uniform cubic- and rhombic-like $LiFePO_4$ particles with sharp corners indicate (nearly) isotropic growth in three directions in the early stage of the hydrothermal reaction.

Results from both sets of theoretical calculations indicate that the surface energy of the (010) and (100) planes is less than that of the (001) plane in the olivine $LiFePO_4$.[28,33] We speculate that the NH_4^+ ions (seen via FTIR) are favorably adsorbed onto the $LiFePO_4$ crystal planes that have higher surface energies (i.e., the (001) faces). This may slow the crystal growth along the *c*-direction. Hence, the speed of crystal growth along the *a*- and *b*-directions becomes similar to that of the *c*-direction. Consequently, crystals that are close to cubic in shape, with sharp edges and corners, are formed as a second morphology.

(V) The cubic and rhombic particles are not thermodynamically stable morphologies and, therefore, evolve to form more thermodynamically stable structures. This process is aided by the presence of the CA, which is used during the hydrothermal synthesis: since CA strongly coordinates Fe^{2+}, it helps to etch (dissolve) the cations from the $LiFePO_4$ crystal surfaces of the particles, allowing the morphologies to continuously evolve. The CA seems to dissolve the Li^+ and Fe^{2+} ions preferentially from the (100) and/or (010) planes, resulting in hollow-structured $LiFePO_4$ single-crystalline particles with holes running along the *a*- and/or *b*-directions. The (001) surface, which is not etched, seems to be one of the more stable surfaces. This may be due to preferential sorption of the NH_4^+ ions on this surface, which may hinder the etching effect of CA. This is a hypothesis that requires further testing, but the stability of the (001) surface is consistent with the slowing of the growth of the particles along this direction, during the earlier stages of the reaction.

Step (v) contains several hypotheses that require further testing. Toward this end, control experiments were conducted to explore the effect of different reagents on the growth mechanisms. To determine the role of NH_4^+ in crystal growth, a series of experiments were carried out by keeping all the parameters

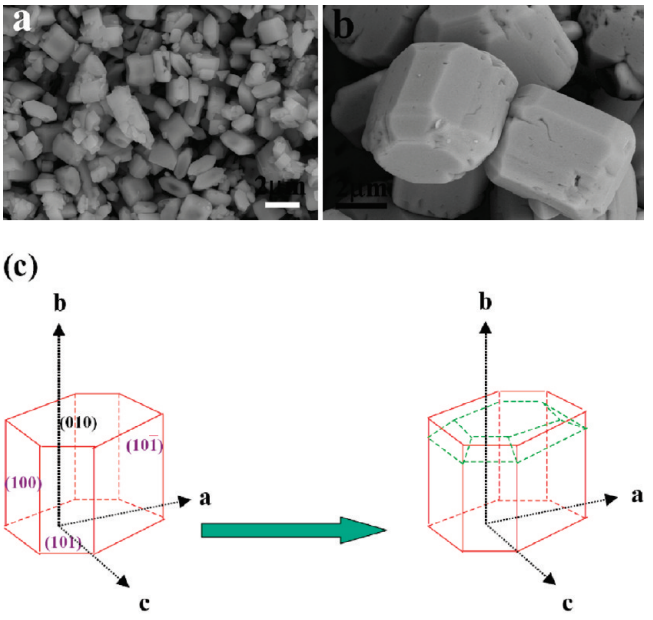

Figure 10. (a, b) Typical SEM images of the $LiFePO_4$ products after hydrothermal reaction for 52 h (panel a) and 120 h (panel b). (c) Schematic showing the transformation of particle morphology from a regular elongated hexagonal-like prism-like to barrel-shaped polyhedral particle shape via the truncation of the edge and corners. The assignment of the face indices are suggestions made based on the calculations presented in ref 28.

constant but without using NH_4^+ ions. The chemical precursors $(NH_4)Fe(SO_4)_2 \cdot H_2O$ and $(NH_4)H_2PO_4$ were replaced by $FeSO_4 \cdot 7H_2O$ and KH_2PO_4, respectively. The XRD analysis, as shown in Figure S7a in the Supporting Information, reveals that single-phase LFP was obtained after 15 h of hydrothermal reaction. However, no cubic-shaped particles were observed by electron microscopy throughout the entire hydrothermal reaction period (from 0.5 h to 24 h) and, instead, the obtained particles displayed a spindle-like morphology (see Figure 9a). No hollow structures were found. All the particles have extremely rough surfaces, particularly the particle indicated by an arrow in Figure 9a. We ascribe these roughened and uneven surface structures to the continuous and random etching effects of CA in the absence of the NH_4^+ ions. $LiFePO_4$ was then prepared without using any CA while keeping all other parameters constant. To maintain the pH value at 7, the $[Li^+]/[Fe^{2+}]$ ratio had to be reduced to 2:1. Figure S7b in the Supporting Information shows the XRD pattern of the obtained product after 15 h of reaction: LFP is present, in addition to a tiny amount of $NH_4FePO_4 \cdot H_2O$, $Li_4P_2O_7$, and Li_3PO_4 secondary phases. However, after 24 h, only LFP is present. In addition to some high-aspect-ratio nanoplates and ultrafine nanoparticles, the sample mainly contains particles with a close to regular cubic shape with sharp edges and corners with mean edge length of ~4 μm, as revealed from Figure 9b. This observation further supports the hypothesis that the selective attachment of the NH_4^+ ion onto the (001) surface favors the formation of cubic-shaped $LiFePO_4$ particles. Furthermore, no hollow structure and roughened/concaved surfaces were seen for these cubes, again suggesting that CA is responsible for the particle etching and the formation of the hollow structures.

3.3.5. Equilibrium Morphology after Hydrothermal Reaction for Longer Times. In order to investigate the stability of the

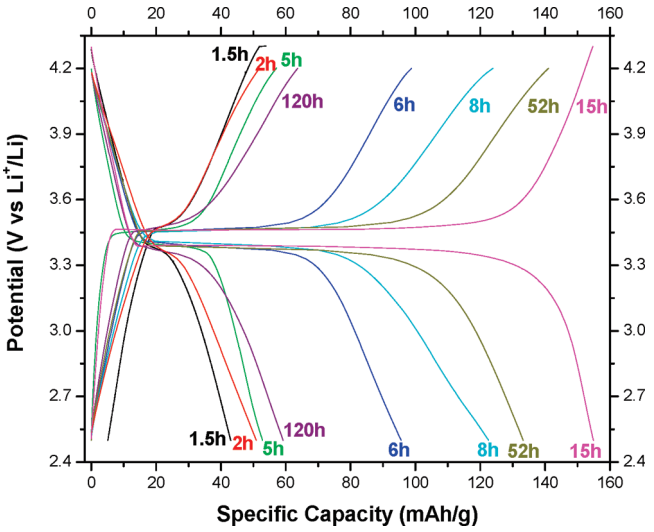

Figure 11. Electrochemical charge and discharge performances of the $LiFePO_4$ samples, as a function of hydrothermal reaction time. The current rate for all the samples was fixed at C/10 based on the theoretical capacity of olivine $LiFePO_4$ (170 mAh/g). All the samples were tested as synthesized without any post-synthesis treatment, except for the 1.5-h sample, which was coated with ~5 wt % of carbon.

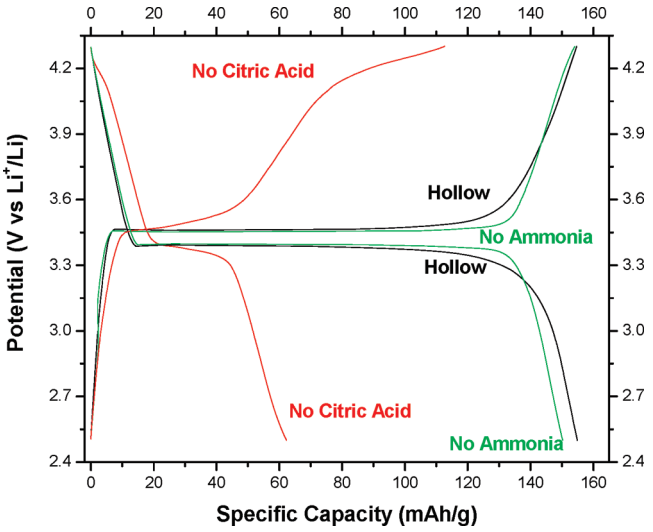

Figure 12. Electrochemical performance comparisons of the $LiFePO_4$ samples synthesized with and without using CA and ammonia in the hydrothermal reaction system, cycled at a C/10 scan rate at room temperature.

hollow particles, the reaction time of the mixture containing both NH_4^+ and CA was further increased. Figure 10a shows the SEM images of the products collected after continuous hydrothermal treatment for 52 h. Most of the particles have lost their hollow structure and the mean crystallite size is reduced to ~1 μm. The hollow morphology is clearly not a thermodynamically stable form under the present experimental conditions.

The reaction was further extended to five days (120 h). Pure olivine phase LFP is still observed (see XRD in Figure S8a in the Supporting Information). But now, as seen from the SEM image in Figure 10b and Figure S8b in the Supporting Information, the particles exhibit a uniform barrel-like morphology with dimensions of ~4 μm × 6 μm. Each barrel-like, single crystal is end-capped by two hexagonal-like faces and terminated by six symmetrically distributed polygon side faces, in addition to some low-index faces resulting from severe truncation on the corner and edges. It is interesting to note that the appearance of the barrel-like particles is quite similar to the calculated equilibrium morphology by Islam et al.[28] Our crystal morphology can be viewed as having evolved from regular elongated hexagonal prism-like crystals after being highly truncated on both the edges and the corners, as schematically illustrated in Figure 10c. This observation also clearly indicates that the previously obtained hollow structure is an intermediate and/or metastable morphology of olivine $LiFePO_4$ crystals synthesized by the current hydrothermal technique. Finally, they transform to this equilibrium barrel-like polyhedral morphology dominated by the {010}, {100}, {101}, and {011} faces.[28]

3.3. Electrochemical Characterization. Poor electrochemistry is observed for the samples collected at the early stages of the hydrothermal reaction and tested, as synthesized, without carbon coating and annealing (see Figure S9 in the Supporting Information). The properties change noticeably after the samples have been annealed and coated with carbon. In particular, the 0-h sample shows a capacity of ~125 mAh/g between 2.1 V to 2.7 V, which may be due to the $Fe_3(PO_4)_2$, a thermal decomposition product of the 0-h sample (see Figure S1b in the Supporting Information). A charge/discharge plateau at ~3.45 V, which is characteristic of LFP, is seen for the 1.5-h sample (see Figure S9 in the Supporting Information and Figure 11), but the capacity is limited (~45 mAh/g between 2.5 V and 4.3 V), compared to the theoretical capacity of olivine LFP (170 mAh/g), presumably because of the disorder observed for this phase (^{31}P NMR), NFP impurities, and the large particle sizes.

The electrochemical performance improves noticeably with reaction time, as clearly demonstrated in Figure 11. Even without carbon coating and heat treatment, the 2-h sample shows a higher specific capacity (~50 mAh/g) than the 1.5-h sample (~42 mAh/g). Although the particle size increases as the reaction time increased from 2 h to 5 h (see Figure 5 and Figure S5 in the Supporting Information), the capacity increases slightly and the charge/discharge polarization decreases, which is ascribed to the enhanced ordering of the crystal structure. The electrochemical activities substantially increase from 6 h to 15 h, achieving a specific capacity of 158 mAh/g at 15 h. The improvement is attributed to the reduction in particle size and the formation of the hollow structures (Figure 6). The hollow structure enhances the contact area between the active materials and the electrolyte, and shortens the diffusion distance for Li^+ throughout the $LiFePO_4$ particle. The hollow morphology may also affect the mechanism of delithiation (e.g., the limits of solid solutions of the end-member phases), and experiments are underway to explore this. After 15 h, the performance drops again as the hollow structure is increasingly lost, even though the particle size decreases for the 52 h sample. After 120 h, the electrochemical reactivity is very limited (~60 mAh/g), presumably because of both the loss of the hollow interior, and the very large grain size (4 μm × 5 μm).

The electrochemical properties of the $LiFePO_4$ particles synthesized with and without the use of CA or ammonia during the hydrothermal reaction are compared in Figure 12. As compared with the hollow sample, $LiFePO_4$ produced in the absence of CA under the conditions used here has a much lower specific capacity (~ 60 mAh/g), lower Coulombic efficiency, and

dx.doi.org/10.1021/cm200205n |Chem. Mater. 2011, 23, 2848–2859

larger polarization, possibly because of the presence of impurities (see Figure S7b in the Supporting Information), and the increase in grain size (see Figure 9b). The LFP particles synthesized in the absence of NH_4^+ displays slightly lower reversible capacity (~150 mAh/g), but interestingly, less polarization and a flatter profile, with a more abrupt change (increase) of the voltage at the very end of charge and discharge. Further experiments are necessary to understand the fundamentals governing this voltage profile. We speculate that it is closely related to the highly roughened surface structure (Figure 9a) resulting from the random etching by CA of this material.

4. CONCLUSIONS

Olivine lithium iron phosphates ($LiFePO_4$, LFP) with a variety of unusual morphologies are prepared in the presence of ammonium (NH_4^+) ions and citric acid (CA). By monitoring the morphologies, we have shown that they eventually transform to a morphology that is similar to that predicted in theoretical studies.[28] The structurally related $NH_4FePO_4 \cdot H_2O$ phase is first formed, transforming to a disordered LFP phase after 1.5 h. The platelet shape of the NFP phase seems to be important in controlling the shape of the first LFP morphology, a poorly defined egg shape. These "eggs" evolve to a mixture of more-symmetric cubes and rhombic particles, whose edges become increasingly well-defined as the reaction time increases to ~5 h. The presence of CA as well as NH_4^+ ions is proposed to be important in determining this particle morphology. Based on our Fourier transform infrared spectroscopy (FTIR) results, NH_4^+ are still present on the surfaces of the LFP particles, and, making use of theoretical studies,[28] we speculate that they are adsorbed preferentially on the {001} surfaces that have higher surface and attachment energies. We suggest that the presence of these ions slows the speed of crystal growth along the *c*-direction, with the Li ions needing to exchange with the NH_4^+ ions before the LFP can grow; consequently, more isotropic LFP particles grow as kinetic products.

As the hydrothermal reaction proceeds, the ability of CA to complex Fe^{2+} and therefore aid in the dissolution (etching) of the LFP, acts a mechanism for the transformation of the kinetic products. Again, we suggest that the CA preferably etches the cubic and rhombic $LiFePO_4$ crystals on the (100) and (010) faces, possibly because more NH_4^+ ions are adsorbed on the (001) surfaces. Hollow LFP particles result after 15 h, with holes running along the [100] and [010] directions, for the cubic and rhombic particles, respectively. These hollow structures are also metastable under the hydrothermal conditions, finally transforming to a barrel-like polyhedral morphology terminated by {010}, {100}, {101}, and {011} faces, which is close to the morphology predicted theoretically based on surface attachment energies.[28] NH_4^+ clearly plays an important role in controlling the morphologies: in its absence, spindle-like LFP particles, with highly roughened surfaces due to random etching by CA (apparently on all the faces) are observed. To the best of our knowledge, these cubic-, rhombic-, and hollow-shaped olivine $LiFePO_4$ single-crystalline particles have not been observed previously. Furthermore, the finding of this type of barrel-like $LiFePO_4$ particle substantiates the prediction by Islam et al.,[28] based on the calculations of surface energetics.

The electrochemical reactivity improves with increasing hydrothermal reaction time, and excellent performance is seen for the hollow particles, even though they are quite large (~1 μm). We suggest that the hollow morphology increases the contact area between the active materials and the electrolyte and reduces the Li^+ diffusion length. The spindle-like LFP with highly roughened surfaces produced in the absence of NH_4^+ also demonstrates very good electrochemical performance, presumably because of its high surface area resulting from the very rough surface structures. Considering their volumetric energy density, these spindle-like $LiFePO_4$ particles are of practical interest. Although the cubic, rhombic, and barrel-like $LiFePO_4$ particles displayed relatively poor electrochemical activity, they provide an interesting platform for the fundamental investigation of the relationship between the particle geometry and electrochemical lithium intercalation and deintercalation mechanisms.

■ ASSOCIATED CONTENT

Supporting Information. Synthetic preparation procedure of single-phase $NH_4FePO_4 \cdot H_2O$; XRD patterns; SEM and TEM images of the samples, as a function of hydrothermal reaction period; a comparison of the crystal structures of $LiFePO_4$ and $NH_4FePO_4 \cdot H_2O$; and the electrochemical profiles of the 0-h, 1-h, and 1.5-h samples. These materials are available free of charge via the Internet at http://pubs.acs.org.

■ AUTHOR INFORMATION

Corresponding Author

*E-mail: cpg27@cam.ac.uk (C.P.G.), appchung@cityu.edu.hk (C.Y.C.).

Present Addresses

○Current address: School of Chemistry and Chemical Engineering, Central South University, Yuelu Campus, Changsha, 410083, PRC.

■ ACKNOWLEDGMENT

This work was financially supported by the Assistant Secretary for Energy Efficiency and Renewable Energy, Office of FreedomCAR and Vehicle Technologies of the U.S. Department of Energy (DOE), under Contract No. DE-AC03-76SF00098 via Subcontract 6517749 with the Lawrence Berkeley National Laboratory. Support also came from the Applied Research Grant of CityU of Hong Kong (No. 9667022), CERG Grant of RGC (No. 1316/03E), and a grant from the Research Grants Council (Project No. CityU 100510) of Hong Kong S.A.R., China. The authors would like to thank Prof. Jonathan Hanson from Brookhaven national Laboratory (BNL) for helpful discussions; assistance during the XRD data collection by Mr. Riza Dervisolgu is gratefully acknowledged. Z.G.L.'s visit to Stony Brook University was funded via a Fulbright Scholarship. Z.G.L. thanks the National Natural Science Foundation of China for a grant (No. 21001117/B0107).

■ REFERENCES

(1) Padhi, A. K.; Nanjundaswamy, K. S.; Goodenough, J. B. *J. Electrochem. Soc.* **1997**, *144*, 1188–1194.

(2) Padhi, A. K.; Nanjundaswamy, K. S.; Masquelier, C.; Okada, S.; Goodenough, J. B. *J. Electrochem. Soc.* **1997**, *144*, 1609–1613.

(3) Tarascon, J. M.; Armand, M. *Nature* **2001**, *414*, 359–367.

(4) Whittingham, M. S. *Chem. Rev.* **2004**, *104*, 4271–4301.

(5) Morgan, D.; Van der Ven, A.; Ceder, G. *Electrochem. Solid State Lett.* **2004**, *7*, A30–A32.

(6) Islam, M. S.; Driscoll, D. J.; Fisher, C. A. J.; Slater, P. R. *Chem. Mater.* **2005**, *17*, 5085–5092.
(7) Ravet, N.; Goodenough, J. B.; Besner, S.; Simoneau, M.; Hovington, P.; Armand, M. In The 196th Meeting of the Electrochemical Society, Honolulu, HI, October 17-22, 1999, Abstract 127No. .
(8) Wilcox, J. D.; Doeff, M. M.; Marcinek, M.; Kostecki, R. *J. Electrochem. Soc.* **2007**, *154*, A389–A395.
(9) Belharouak, I.; Johnson, C.; Amine, K. *Electrochem. Commun.* **2005**, *7*, 983–988.
(10) Xie, H. M.; Wang, R. S.; Ying, J. R.; Zhang, L. Y.; Jalbout, A. F.; Yu, H. Y.; Yang, G. L.; Pan, X. M.; Su, Z. M. *Adv. Mater.* **2006**, *18*, 2609.
(11) Huang, Y. H.; Park, K. S.; Goodenough, J. B. *J. Electrochem. Soc.* **2006**, *153*, A2282–A2286.
(12) Lu, Z. G.; Cheng, H.; Lo, M. F.; Chung, C. Y. *Adv. Funct. Mater.* **2007**, *17*, 3885–3896.
(13) Herle, P. S.; Ellis, B.; Coombs, N.; Nazar, L. F. *Nat. Mater.* **2004**, *3*, 147–152.
(14) Hu, Y. S.; Guo, Y. G.; Dominko, R.; Gaberscek, M.; Jamnik, J.; Maier, J. *Adv. Mater.* **2007**, *19*, 1963.
(15) Kang, B.; Ceder, G. *Nature* **2009**, *458*, 190–193.
(16) Chung, S. Y.; Bloking, J. T.; Chiang, Y. M. *Nat. Mater.* **2002**, *1*, 123–128.
(17) Yamada, A.; Chung, S. C.; Hinokuma, K. *J. Electrochem. Soc.* **2001**, *148*, A224–A229.
(18) Delacourt, C.; Poizot, P.; Levasseur, S.; Masquelier, C. *Electrochem. Solid State Lett.* **2006**, *9*, A352–A355.
(19) Gaberscek, M.; Dominko, R.; Bele, M.; Remskar, M.; Hanzel, D.; Jamnik, J. *Solid State Ionics* **2005**, *176*, 1801–1805.
(20) Doherty, C. M.; Caruso, R. A.; Smarsly, B. M.; Drummond, C. J. *Chem. Mater.* **2009**, *21*, 2895–2903.
(21) Lim, S. Y.; Yoon, C. S.; Cho, J. P. *Chem. Mater.* **2008**, *20*, 4560–4564.
(22) Srinivasan, V.; Newman, J. *J. Electrochem. Soc.* **2004**, *151*, A1517–A1529.
(23) Laffont, L.; Delacourt, C.; Gibot, P.; Wu, M. Y.; Kooyman, P.; Masquelier, C.; Tarascon, J. M. *Chem. Mater.* **2006**, *18*, 5520–5529.
(24) Chen, G. Y.; Song, X. Y.; Richardson, T. J. *Electrochem. Solid State Lett.* **2006**, *9*, A295–A298.
(25) Ramana, C. V.; Mauger, A.; Gendron, F.; Julien, C. M.; Zaghib, K. *J. Power Sources* **2009**, *187*, 555–564.
(26) Andersson, A. S.; Thomas, J. O. *J. Power Sources* **2001**, *97*−*98*, 498–502.
(27) Delmas, C.; Maccario, M.; Croguennec, L.; Le Cras, F.; Weill, F. *Nat. Mater.* **2008**, *7*, 665–671.
(28) Fisher, C. A. J.; Islam, M. S. *J. Mater. Chem.* **2008**, *18*, 1209–1215.
(29) Ellis, B.; Kan, W. H.; Makahnouk, W. R. M.; Nazar, L. F. *J. Mater. Chem.* **2007**, *17*, 3248–3254.
(30) Wagemaker, M.; Mulder, F. M.; Van der Ven, A. *Adv. Mater.* **2009**, *21*, 2703–2709.
(31) Dokko, K.; Koizumi, S.; Nakano, H.; Kanamura, K. *J. Mater. Chem.* **2007**, *17*, 4803–4810.
(32) Ferrari, S.; Lavall, R. L.; Capsoni, D.; Quartarone, E.; Magistris, A.; Mustarelli, P.; Canton, P. *J. Phys. Chem. C* **2010**, *114*, 12598–12603.
(33) Wang, L.; Zhou, F.; Meng, Y. S.; Ceder, G. *Phys. Rev. B* **2007**, *76*, 165435.
(34) Nishimura, S.; Kobayashi, G.; Ohoyama, K.; Kanno, R.; Yashima, M.; Yamada, A. *Nat. Mater.* **2008**, *7*, 707–711.
(35) Amin, R.; Balaya, P.; Maier, J. *Electrochem. Solid State Lett.* **2007**, *10*, A13–A16.
(36) Li, J. Y.; Yao, W. L.; Martin, S.; Vaknin, D. *Solid State Ionics* **2008**, *179*, 2016–2019.
(37) Malik, R.; Burch, D.; Bazant, M.; Ceder, G. *Nano Lett.* **2010**, *10*, 4123–4127.
(38) Jones, J. L.; Hung, J. T.; Meng, Y. S. *J. Power Sources* **2009**, *189*, 702–705.
(39) Arico, A. S.; Bruce, P.; Scrosati, B.; Tarascon, J. M.; Van Schalkwijk, W. *Nat. Mater.* **2005**, *4*, 366–377.
(40) Wang, G.; Shen, X.; Yao, J. *J. Power Sources* **2009**, *189*, 543–546.
(41) Recham, N.; Dupont, L.; Courty, M.; Djellab, K.; Larcher, D.; Armand, M.; Tarascon, J. M. *Chem. Mater.* **2009**, *21*, 1096–1107.
(42) Murugan, A. V.; Muraliganth, T.; Manthiram, A. *J. Phys. Chem. C* **2008**, *112*, 14665–14671.
(43) Saravanan, K.; Reddy, M. V.; Balaya, P.; Gong, H.; Chowdari, B. V. R.; Vittal, J. J. *J. Mater. Chem.* **2009**, *19*, 605–610.
(44) Chen, J.; Wang, S.; Whittingham, M. S. *J. Power Sources* **2007**, *174*, 442–448.
(45) Yang, S. F.; Zavalij, P. Y.; Whittingham, M. S. *Electrochem. Commun.* **2001**, *3*, 505–508.
(46) Recham, N.; Armand, M.; Laffont, L.; Tarascon, J. M. *Electrochem. Solid State Lett.* **2009**, *12*, A39–A44.
(47) Dokko, K.; Koizumi, S.; Kanamura, K. *Chem. Lett.* **2006**, *35*, 338–339.
(48) Franger, S.; Le Cras, F.; Bourbon, C.; Rouault, H. *J. Power Sources* **2003**, *119*, 252–257.
(49) Xu, C. B.; Lee, J.; Teja, A. S. *J. Supercrit. Fluids* **2008**, *44*, 92–97.
(50) Wang, Z. L.; Su, S. R.; Yu, C. Y.; Chen, Y.; Xia, D. G. *J. Power Sources* **2008**, *184*, 633–636.
(51) Qian, J. F.; Zhou, M.; Cao, Y. L.; Ai, X. P.; Yang, H. X. *J. Phys. Chem. C* **2010**, *114*, 3477–3482.
(52) Wang, Y.; Wang, Y.; Hosono, E.; Wang, K.; Zhou, H. *Angew. Chem., Int. Ed.* **2008**, *47*, 7461–7465.
(53) Lee, M.-H.; Kim, J.-Y.; Song, H.-K. *Chem. Commun.* **2010**, *46*, 6795–6797.
(54) Yang, H.; Wu, X. L.; Cao, M. H.; Guo, Y. G. *J. Phys. Chem. C* **2009**, *113*, 3345–3351.
(55) Chen, J. J.; Whittingham, M. S. *Electrochem. Commun.* **2006**, *8*, 855–858.
(56) Meligrana, G.; Gerbaldi, C.; Tuel, A.; Bodoardo, S.; Penazzi, N. *J. Power Sources* **2006**, *160*, 516–522.
(57) Hsu, K. F.; Tsay, S. Y.; Hwang, B. J. *J. Mater. Chem.* **2004**, *14*, 2690–2695.
(58) Uchiyama, H.; Imai, H. *Cryst. Growth Des.* **2010**, *10*, 1777−1781.
(59) Carling, S. G.; Day, P.; Visser, D. *Inorg. Chem.* **1995**, *34*, 3917–3927.
(60) Zhao, Y.; Li, F.; Zhang, R.; Evans, D. G.; Duan, X. *Chem. Mater.* **2002**, *14*, 4286–4291.
(61) Kim, J.; Nelson, U. G.; Grey, C. P. *J. Am. Chem. Soc.* **2008**, *130*, 1285–1295.
(62) Hamelet, S.; Gibot, P.; Casas-Cabanas, M.; Bonnin, D.; Grey, C. P.; Cabana, J.; Leriche, J. B.; Rodriguez-Carvajal, J.; Courty, M.; Levasseur, S.; Carlach, P.; Thournout, M. V.; Tarascon, J. M.; Masquelier, C. *J. Mater. Chem.* **2009**, *19*, 3979–3991.
(63) Kim, J.; Middlemiss, D. S.; Chernova, N. A.; Zhu, B. Y. X.; Masquelier, C.; Grey, C. P. *J. Am. Chem. Soc.* **2010**, *132*, 16825–16840.
(64) Tucker, M. C.; Doeff, M. M.; Richardson, T. J.; Finones, R.; Cairns, E. J.; Reimer, J. A. *J. Am. Chem. Soc.* **2002**, *124*, 3832–3833.
(65) Wilcke, S. L.; Lee, Y. J.; Cairns, E. J.; Reimer, J. A. *Appl. Magn. Reson.* **2007**, *32*, 547–563.
(66) Tucker, M. C.; Doeff, M. M.; Richardson, T. J.; Finones, R.; Reimer, J. A.; Cairns, E. J. *Electrochem. Solid State Lett.* **2002**, *5*, A95–A98.
(67) Cabana, J.; Shirakawa, J.; Chen, G. Y.; Richardson, T. J.; Grey, C. P. *Chem. Mater.* **2010**, *22*, 1249–1262.
(68) Kim, J.; Grey, C. P. *Chem. Mater.* **2010**, *22*, 5453–5462.
(69) Yuan, A. Q.; Wu, J.; Huang, Z. Y.; Wu, K.; Liao, S.; Tong, Z. E. *Mater. Res. Bull.* **2008**, *43*, 1339–1345.
(70) Marx, N.; Croguennec, L.; Carlier, D.; Bourgeois, L.; Kubiak, P.; Cras, F. L.; Delmas, C. *Chem. Mater.* **2010**, *22*, 1854–1861.
(71) Long, R. Q.; Yang, R. T. *J. Catal.* **2000**, *190*, 22–31.
(72) Ravet, N.; Gauthier, M.; Zaghib, K.; Goodenough, J. B.; Mauger, A.; Gendron, F.; Julien, C. M. *Chem. Mater.* **2007**, *19*, 2595–2602.
(73) Maccario, M.; Croguennec, L.; Desbat, B.; Couzi, M.; Le Cras, F.; Servant, L. *J. Electrochem. Soc.* **2008**, *155*, A879–A886.

(74) Burba, C. M.; Frech, R. *J. Electrochem. Soc.* **2004**, *151*, A1032–A1038.
(75) Li, W.; Gao, J.; Ying, J. R.; Wan, C. R.; Jiang, C. Y. *J. Electrochem. Soc.* **2006**, *153*, F194–F198.
(76) Chen, J. J.; Vacchio, M. J.; Wang, S. J.; Chernova, N.; Zavalij, P. Y.; Whittingham, M. S. *Solid State Ionics* **2008**, *178*, 1676–1693.
(77) Uchiyama, H.; Imai, H. *Cryst. Growth Des.* **2010**, *10*, 1777–1781.